Polarization-enabled spectral-focusing CARS microscopy

R. A. COLE AND A. D. SLEPKOV[*] (iD)

Department of Physics and Astronomy, Trent University, 1600 W Bank Dr., Peterborough, Ontario, K9L 0G2, Canada
[*]*aaronslepkov@trentu.ca*

Abstract: We describe a spectral-focusing-based polarization-resolved coherent anti-Stokes Raman scattering (SFP-CARS) microscopy system developed by making simple and inexpensive modifications to an existing spectral focusing CARS setup. By using the system to study polarization dependent features in the CARS spectrum of benzonitrile, we assess its capabilities and demonstrate its ability to accurately determine Raman depolarization ratios. Ultimately, the detected anti-Stokes signals are more elliptically polarized than expected, hindering a complete suppression of the non-resonant background. Furthermore, the fact that resonant signals polarized in directions similar to that of the non-resonant background are also substantially suppressed when extinguishing the non-resonant background remains a serious limitation. We conclude that non-resonant background suppression using the SFP-CARS system is best suited for studying Raman modes that generate signals polarized in directions far from that of the non-resonant background instead of for obtaining background-free CARS spectra. In all, we find that the SFP-CARS setup is a useful tool for studying polarization dependent features in the CARS spectra of various samples that is worthy of further investigation. This work aims to illuminate several technical aspects of polarization dependent CARS and inform researchers of the benefits and constraints of integrating polarization dependent detection as an add-on to existing CARS microscopy setups.

1. Introduction

Coherent anti-Stokes Raman scattering (CARS) microscopy is a four-wave mixing (FWM) technique with widespread applications in fields such as biomedicine, materials characterization, and biological imaging [1,2]. This powerful imaging tool uses the intrinsic vibrational resonances of molecules to provide label-free and chemically specific imaging, making it appealing for researchers interested in studying samples without alteration using dyes or labels [1,2]. Conventional CARS microscopy involves the detection of anti-Stokes light generated via the nonlinear optical interaction of at least two laser pulses in a sample—a degenerate pump/probe and a Stokes, with central frequencies of ω_p and ω_s respectively [3,4]. The anti-Stokes (AS) signal, of frequency $\omega_{AS} = 2\omega_p - \omega_s$, is resonantly enhanced when the difference between the pump and Stokes frequencies corresponds to a Raman active vibrational mode in the sample, $\omega_R = \omega_p - \omega_s$, thus providing the chemically specific contrast mechanism exploited in CARS microscopy [3,4].

Several strategies exist for experimentally implementing CARS, each having their own advantages and disadvantages. Spectral focusing (SF) CARS is a particular approach that is gaining in popularity due in part to its reliance on broadband laser pulses [5]. This allows for the concurrent integration of other nonlinear optical microscopy techniques that require high pulse intensities, such as second harmonic generation (SHG) and two-photon excitation fluorescence (TPEF), in a combination referred to as "multimodal" [6–9]. In SF-CARS, broadband fs pump and Stokes pulses are temporally dispersed such that the rate of change of each pulse's instantaneous frequency with time (i.e. their "chirps") is made equal. The instantaneous frequency difference

of these chirp-matched pulses has substantially narrower bandwidth compared to the bandwidths of the pump and Stokes pulses, resulting in significantly improved CARS spectral resolution and signal intensity [10,11]. Furthermore, once chirp-matching is established, scanning Raman frequencies is easily accomplished by varying the temporal overlap of the pump and Stokes pulses. This allows for rapid acquisition of the CARS spectrum at each pixel, a combination referred to as "hyperspectral imaging" [12–15]. The multimodal and hyperspectral capabilities of SF-CARS are making this technique an increasingly attractive approach for researchers looking to exploit the many benefits of CARS microscopy.

While there are many benefits of CARS microscopy, the technique is not without its share of drawbacks and difficulties; the presence of a non-resonant background (NRB) chief among them [16]. Many strategies to suppress the NRB have been implemented over the past two decades, including time-resolved CARS [17–19], the use of phase-retrieval algorithms [20–22], and polarization-resolved CARS (P-CARS) [23,24]. P-CARS is an earlier approach that has more recently been used to study the organization and orientation of molecules within samples [25,26]. P-CARS has also been used to determine the Raman depolarization ratios of various Raman resonances within samples, thereby providing insight into the symmetries of molecular vibrations [27,28].

As with many CARS techniques, P-CARS is often implemented using ps pump and Stokes pulses because their inherent bandwidths match the natural linewidths of ambient molecular vibrations, resulting in a good balance of resonant signal strength and contrast over the NRB [4,29]. However, the need to vary either the pump or Stokes wavelengths to probe different Raman modes means that it is often significantly time-consuming to collect rich hyperspectral P-CARS signals. P-CARS has also been performed with broadband approaches such as multiplex-CARS, where wide regions of a sample's Raman spectrum are probed simultaneously and the resulting CARS signals are detected using a spectrometer [28,30]. While this approach facilitates rapid collection of P-CARS data over a broad spectral range, spectral acquisition times on the order of ms limits the image acquisition speed of conventional multiplex-CARS systems to several minutes [31], and the addition of polarization sensitive detection can easily increase this to tens of minutes. Since SF-CARS offers perhaps the greatest flexibility among CARS techniques to switch between high-speed, on-resonance imaging and good quality acquisition of CARS spectra, the feasibility, potential benefits, and difficulties of implementing P-CARS with a spectral-focusing-based setup are important and timely avenues of investigation.

In this work, we explore the capabilities of a spectral-focusing-based polarization-resolved CARS (SFP-CARS) microscopy system developed by modifying our existing SF-CARS system, first reported in [6]. We discuss the feasibility, advantages, and disadvantages of adding polarization dependent detection to our existing SF-CARS setup with minimal economic cost. We assess the capabilities of the newly developed SFP-CARS system by studying polarization dependent features in the CARS spectrum of benzonitrile as a model reference material. We find that while the detected CARS signals are weaker in the polarization enabled approach, compared with the original SF-CARS setup (as expected from P-CARS theory [16]), most are still well within our detection limits. Furthermore, the CARS signals appear to be more elliptically polarized than expected, likely due to microscope and collection optics distorting the polarizations of the generated signals on route to the detector. These polarization distortions also appear to hinder the ability of the SFP-CARS system to suppress the NRB. Nevertheless, despite these shortcomings, we show that the SFP-CARS system can be used to determine the Raman depolarization ratios of various Raman resonances in benzonitrile with a high degree of accuracy. In this way, we report on a unique implementation of polarization dependent detection in SF-CARS microscopy. In doing so, we aim to inform a diverse range of researchers of the considerations involved in integrating polarization dependent detection as an add-on to existing

SF-CARS systems, as well as to provide valuable insight as to the nature and implementation of P-CARS for the broader nonlinear microscopy community.

2. Overview of P-CARS theory

A nonlinear polarization is induced when the pump and Stokes beams involved in CARS are focused in a sample [32]. The component of this nonlinear polarization responsible for light emitted at the AS frequency, ω_{AS}, comprises two terms: a resonant term, $\mathbf{P}_{AS}^{(3)R}$, which is enhanced when the difference between the pump and Stokes frequencies corresponds to a Raman active vibrational mode in the sample, and a non-resonant term, $\mathbf{P}_{AS}^{(3)NR}$, which is present regardless of the difference between the pump and Stokes frequencies (where the superscript "(3)" refers to the fact that these terms originate from the third-order nonlinear polarization) [2]. AS signal arising from $\mathbf{P}_{AS}^{(3)NR}$ limits the sensitivity of CARS techniques and thus comprises the NRB. Moreover, for techniques such as SF-CARS where vibrational spectra are obtained, the NRB leads to spectral reshaping and distortions of the equivalent spontaneous Raman spectrum [33]. This complicates the direct comparisons of CARS and Raman spectra.

P-CARS is a variant capable of suppressing the NRB by exploiting the difference between the polarizations of the generated non-resonant and resonant AS signals [24]. The generalized scheme is as follows [23,24]: Consider pump and Stokes beams, of frequencies ω_p and ω_s respectively, propagating in the z direction and focused on a sample. The pump beam is linearly polarized along the x-axis while the Stokes beam is linearly polarized at an angle ϕ relative to the x-axis. Under these circumstances, the generated non-resonant and resonant AS signals are both linearly polarized at angles α and β relative to the x-axis, respectively [4], as depicted in Fig. 1. In principle, the non-resonant signal can then be extinguished by placing an analyzer (polarizer) with a transmission axis perpendicular to $\mathbf{P}_{AS}^{(3)NR}$ after the sample [23]. In practice, complete extinction of the NRB is prevented because of polarization distortions caused by tight beam focusing in the microscope, as well as by optics in the signal's path on route to the detector [24].
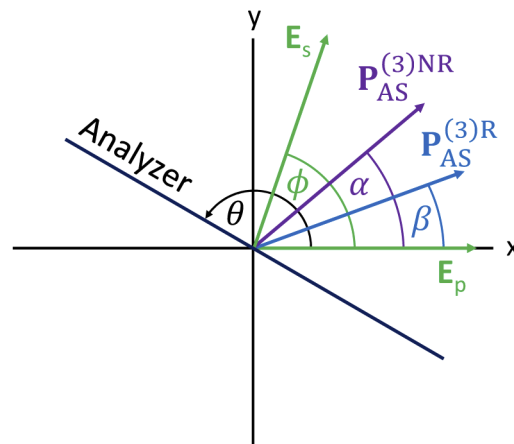

Fig. 1. An illustration defining the polarization directions of the pump ($\mathbf{E}_p$), Stokes ($\mathbf{E}_s$), non-resonant anti-Stokes ($\mathbf{P}_{AS}^{(3)NR}$), and resonant anti-Stokes ($\mathbf{P}_{AS}^{(3)R}$) signals along with the transmission axis of the analyzer.

Provided that the pump and Stokes frequencies are far from single-photon electronic resonances of the sample, the depolarization ratio of the non-resonant AS signal, ρ_{NR}, is equal to 1/3 [34]. Cheng *et al.* [24] showed that under this condition the maximum vibrational contrast while extinguishing the NRB with the analyzer is obtained when the difference between the pump and Stokes polarizations is $\phi \approx 71.6°$, resulting in non-resonant AS signals polarized at $\alpha = 45°$ (with

respect to the pump polarization). The depolarization ratio of the resonant AS signal, ρ_R, is equal to the spontaneous Raman depolarization ratio of the corresponding resonance and lies within the range $0 \leq \rho_R \leq 0.75$ [4]. ρ_R depends on the symmetry of the corresponding molecular vibration, having a value of 0 for totally symmetric vibrational modes and a value of 0.75 for entirely depolarized modes [34]. The depolarization ratios of the non-resonant and resonant AS signals are related to the corresponding polarization directions, α and β, and the angle between the pump and Stokes polarizations, ϕ, by [4]

$$\rho_{NR} = \frac{\tan(\alpha)}{\tan(\phi)} \tag{1}$$

and

$$\rho_R = \frac{\tan(\beta)}{\tan(\phi)}. \tag{2}$$

It should be noted that for cases where $\rho_R = \rho_{NR}$, $\beta = \alpha$ and thus the non-resonant signal cannot be extinguished by the analyzer without simultaneously extinguishing the resonant signal. For this reason, suppression of non-resonant signals by polarization filtering is most beneficial for studying resonances with depolarization ratios far from $\rho_R = 1/3$.

From Fig. 1, it is clear that after passing through the analyzer with a transmission axis oriented at angle θ relative to the x-axis the intensities of the non-resonant and resonant AS signals are given in accordance with Malus' law by $I_{AS}^{NR}(\theta) = I_{AS_0}^{NR} \cos^2(\alpha - \theta)$ and $I_{AS}^{R}(\theta) = I_{AS_0}^{R} \cos^2(\beta - \theta)$, respectively (where $I_{AS_0}^{NR}$ and $I_{AS_0}^{R}$ are the intensities of the non-resonant and resonant AS signals before the analyzer). Note that $I_{AS_0}^{NR} \propto |\chi^{(3)NR}|^2$ and $I_{AS_0}^{R} \propto |\chi^{(3)R}|^2$, where $\chi^{(3)NR}$ and $\chi^{(3)R}$ are the corresponding non-resonant and resonant third order nonlinear optical susceptibilities [35]. Since CARS is a coherent process, the non-resonant and resonant signals interfere, and thus the total intensity of the AS signal after passing through the analyzer rotated at angle θ relative to the x-axis is given by

$$I_{AS}^{Tot}(\theta) = I_{AS_0}^{NR} \cos^2(\alpha - \theta) + 2\cos(\delta)\sqrt{I_{AS_0}^{NR}}\sqrt{I_{AS_0}^{R}}\cos(\alpha - \theta)\cos(\beta - \theta) + I_{AS_0}^{R}\cos^2(\beta - \theta), \tag{3}$$

where δ in the central "interference" term is the phase difference between the resonant and non-resonant AS signal amplitudes. It is worth noting that the total AS signal is generally elliptically polarized, both because of this phase difference and because of the differing polarization directions of the resonant and non-resonant signals [36]. As such, the signal cannot be completely extinguished by the analyzer. When the difference between the pump and Stokes frequencies does not correspond to a Raman active vibrational mode, the terms in Eq. (3) that contain a resonant contribution vanish and the intensity of the entirely non-resonant signal passing through the analyzer is given by

$$I_{AS}^{NR}(\theta) = I_{AS_0}^{NR} \cos^2(\alpha - \theta). \tag{4}$$

When the difference between the pump and Stokes frequencies does correspond to a Raman resonance, all terms in Eq. (3) generally contribute to the total AS signal intensity. However, for concentrated samples with large Raman scattering cross sections $I_{AS_0}^{R} \gg I_{AS_0}^{NR}$, and the third term in Eq. (3) is the dominant contributor to the total AS signal intensity while the remaining two terms have the effect of shifting the minimum value of $I_{AS}^{Tot}(\theta)$ as a function of θ to some value above zero. Thus, for cases where $I_{AS_0}^{R} \gg I_{AS_0}^{NR}$, Eq. (3) can be approximated by a modified version of Malus' law given by

$$I_{AS}^{Tot}(\theta) \approx I_{AS_0}^{R} \cos^2(\beta - \theta) + C, \tag{5}$$

where C is a complicated function of α, β, δ, $I_{AS_0}^{NR}$, and $I_{AS_0}^{R}$ that does not depend on θ. Note that the first two terms of Eq. (3) also have the effect of introducing a slight phase shift, but this phase

shift is negligible under the assumption of strong resonance and is thus omitted from within the $\cos^2$ term in Eq. (5).

By measuring the intensity of the on-resonance AS signal as a function of analyzer angle and fitting the data to Eq. (5), one can determine the polarization angle of the resonant signal, β. With this, we see that Eq. (2) can then be used to determine the corresponding Raman depolarization ratio. While Eq. (5) may seem like a coarse approximation of $I_{\mathrm{AS}}^{\mathrm{Tot}}(\theta)$, by comparing Eq. (5) with Eq. (3) we estimate that a Raman depolarization ratio determined in this way will be within 0.1 of its true value if the Raman resonance satisfies $|\chi^{(3)\mathrm{R}}| > 10|\chi^{(3)\mathrm{NR}}|$ [37], assuming that $\alpha = 45°$ and thus $\phi \approx 71.6°$ [24]. (Note that the value of 0.1 is determined under the assumption of maximum interference between the non-resonant and resonant signals and thus generally overestimates the error in Raman depolarization ratios determined using this approach.) For strong Raman resonances, such as those originating from concentrated samples, this approach is a simple, accurate, and reliable means of determining the corresponding Raman depolarization ratios. We highlight this in the results section by demonstrating the effectiveness of using Eq. (5) in combination with Eq. (2) to determine the Raman depolarization ratios of various Raman resonances in benzonitrile. Nevertheless, for weak Raman resonances where $|\chi^{(3)\mathrm{R}}|$ is comparable to, or less than, $|\chi^{(3)\mathrm{NR}}|$, determining depolarization ratios by fitting the total AS signal intensity to Eq. (5) can result in significant error. In such cases, techniques such as phase-retrieval algorithms should be used to separate the non-resonant and resonant AS signal intensities [22]. The resonant AS signal intensity, as opposed to the total AS signal intensity, can then be safely fitted to Eq. (5) to extract the value of β and determine the corresponding Raman depolarization ratio. In this way, P-CARS can be used to determine the Raman depolarization ratios of various Raman resonances. When implemented in a microscope, the resonances and depolarization ratios can be mapped spatially, potentially offering important information with regards to local molecular orientation and organization.

3. Experiment

A schematic of the SFP-CARS setup is given in Fig. 2. A Ti:Sapphire oscillator generates a beam of 800 nm, 100 fs pulses that is separated into two paths: one serving as the degenerate pump/probe (henceforth: "pump") beam and the other becoming the Stokes beam. The pump is sent to a computer-controlled optical delay stage before recombining with the Stokes. The other beam is coupled into a commercial photonic crystal fiber (PCF) supercontinuum generation module (FemtoWHITE-CARS, NKT Photonics) using a 40× objective lens to generate the Stokes beam. The throughput/coupling efficiency of the PCF is approximately 50%. A Mitutoyo (M Plan NIR 50×) long-working-distance objective is used to collimate the Stokes beam. The two beams are combined using an angled dichroic mirror (Chroma T810lpxr) acting as an 810 nm long-pass filter and directed via a periscope into the microscope.

To enable spectral focusing, the pump and Stokes beams are sent through a total of 101 mm and 158 mm of S-NPH2 glass respectively, to both disperse and chirp-match the pulses. This arrangement allows for probing Raman modes from ~850 cm^{-1} to ~3200 cm^{-1} in a single temporal scan. The resulting spectral resolution is ~30 cm^{-1} in the middle of this range (around 2000 cm^{-1}). As discussed previously, the Stokes is predominantly linearly chirped and we do not find the spectral resolution to vary substantially across the observable CARS spectrum [6,10].

The microscope is a modified Olympus IX73 inverted laser-scanning microscope with a 0.30 NA 10× objective (Olympus UMPLFLN10XW), a Thorlabs scanning galvo system, and a computerized x-y sample stage. A low NA 10× objective is chosen for in this work because higher NA objectives used in our previously reported work [6] cause greater polarization distortions [34]. We find that the reduced CARS signals obtained by using the smaller NA objective represents a lower barrier to this research than the polarization distortions of the higher-NA objectives. The generated AS signals are collected in the forward direction, sent through a linear polarizer
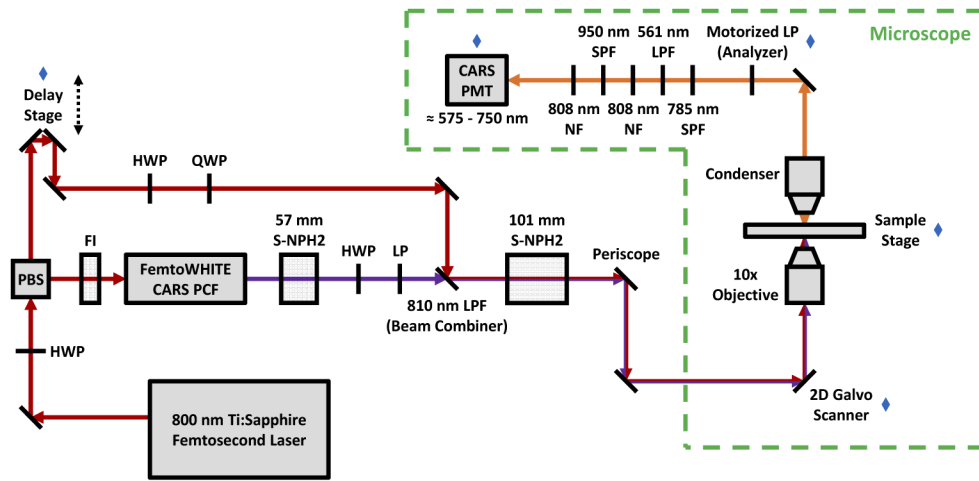
Fig. 2. A schematic of the SFP-CARS microscopy setup. A Ti:Sapphire oscillator generates a beam of 800 nm, 100 fs pulses. A half-wave plate (HWP) and polarizing beam splitter (PBS) act as a variable beam splitter to create the pump and Stokes-generating arms. The pump beam is sent to a computer-controlled optical delay stage before recombining with the Stokes. The Stokes-generating beam is sent through a Faraday isolator (FI) before being coupled into a FemtoWHITE CARS (NKT Photonics) module to generate the Stokes supercontinuum. Blocks of high-dispersion S-NPH2 glass are used to temporally disperse and chirp-match the pump and Stokes pulses. The pump and Stokes beams are recombined using an angled dichroic mirror effectively acting as an 810 nm long-pass filter (LPF) and sent to the laser-scanning microscope. The generated AS signals are collected in the forward direction, sent through a motorized linear polarizer (LP), and detected by a PMT. A collection of short-pass filters (SPF), notch filters (NF), and LPFs are placed between the analyzer and the PMT to isolate the AS signals. A HWP and a quarter-wave plate (QWP) are placed in the pump path while a HWP and a LP are placed in the Stokes path to control the polarizations of the pump and Stokes beams. The blue diamonds indicate elements that are computer controlled and synchronized by a custom Python program.

acting as the analyzer that is mounted in a computer-controlled motorized rotation mount, and detected by a PMT (Hamamatsu H10723-20). A collection of short-pass, long-pass, and notch filters are placed in the AS signal's path between the analyzer and the PMT to filter out other nonlinear optical signals in addition to unwanted pump and Stokes signals as depicted in Fig. 2. Alternatively, the AS signals can be sent to a portable USB spectrometer instead of the PMT to calibrate the Raman mode probed as a function of pump delay stage position.

To control the polarizations of the incident beams, a half-wave plate and a quarter-wave plate are placed in the pump beam path after the delay stage while a half-wave plate and a linear polarizer are placed in the Stokes beam path before the beam combiner. The quarter-wave plate in the pump beam path is needed to compensate for the birefringence of the beam combiner and the polarization distortions caused by the periscope. The Stokes beam is sufficiently linearly polarized without the addition of a quarter-wave plate. However, a linear polarizer is needed in the Stokes beam path because the PCF module is not polarization maintaining and, as we've recently shown, outputs a supercontinuum with complicated polarization properties [38]. The extinction ratios of the pump (ER_p) and Stokes (ER_s) beams and the angle between the pump and Stokes polarizations (ϕ) are measured to be approximately $ER_p \approx 23{:}1$, $ER_s \approx 52{:}1$, and $\phi \approx 75°$ at the location of the analyzer with no sample in the microscope.

Complete experimental control and data acquisition was carried out using a single custom Python computer program. In all, the notable modifications needed to transform the SF-CARS setup reported in [6] into the SFP-CARS setup described in this work include the additions of the quarter-wave plate in the pump beam path, the linear polarizer in the Stokes beam path, and the analyzer after the sample; the removal of a dichroic mirror used for collecting signals generated in the epi-direction (which was causing significant distortions to the polarizations of the incident pump and Stokes beams); and the placement of the PMT and all filters in the signals' path immediately after the analyzer. Whereas our typical SF-CARS setup employs a custom multimode fiber adapter that routes transmitted (CARS/SHG) signals to off-board detectors [8], the needs for strict polarization control in this work required the detection system to be affixed on-board the microscope frame.

Benzonitrile was chosen as a test sample because of its collection of strong and isolated Raman modes that have a variety of Raman depolarization ratios and span a wide range of frequencies. CARS spectra were obtained from benzonitrile in a microscope well slide by collecting a hyperspectral stack of 30×30 pixel images while continually scanning the pump delay stage, yielding a set of images as a function of delay stage position. Delay stage position is then converted to vibrational frequency via calibration by monitoring the frequency of the AS signal generated from an empty glass slide as detailed in [6]. To obtain intensity as a function of vibrational frequency, the average pixel intensity of each image is used to give a single intensity value for each image. The pump and Stokes powers entering the microscope were approximately 100 mW and 7.0 mW, respectively. 46 CARS spectra spanning 850 cm^{-1} to 3200 cm^{-1} were obtained; one at each analyzer angle within a 180° range in 4° increments. Additionally, the pump and Stokes intensities reaching the detector at each analyzer angle were subtracted from the corresponding benzonitrile spectra to remove pump and Stokes leakage. To determine the analyzer angle that corresponds to the polarization of the pump beam and thus calibrate the $\theta = 0°$ analyzer angle, the Stokes beam was blocked and the pump intensity reaching the detector was measured at each of the 46 analyzer angles. The measured pump intensity was then plotted as a function of analyzer angle and fitted to Malus' law to extract the analyzer angle that best matches the maximum pump transmission ($\theta = 0°$). It took roughly 100 s to obtain each benzonitrile CARS spectrum, with a pixel dwell time of ~95 μs and a pump delay stage movement speed of 0.05 mm/s. Thus, a full polarization dependent hyperspectral scan sequence took approximately 80 minutes. Note that we prioritized high quality results over acquisition speed for this diagnostic and exploratory study and thus the 100 s spectral acquisition time is not indicative of the maximum possible acquisition speed. We estimate that reasonable quality spectra could be obtained in half the time by reducing the pixel dwell time, thereby lowering the time needed to obtain spectra at the 46 polarization settings to less than 40 minutes. The spectral acquisition time could be further reduced by scanning a narrower portion of the Raman spectrum. If only a single Raman resonance is studied such that the pump delay stage remains fixed, then we estimate that all 46 images (one at each analyzer angle) could be obtained in less than a couple of minutes.

4.   Results and discussion

An animation of the benzonitrile CARS spectrum obtained at various analyzer angles is given in Visualization 1. This animation highlights the different polarizations of the emerging CARS signals at various vibrational modes in benzonitrile. The minute-to-minute instabilities in the Stokes spectrum are observable as fluctuation of sequential spectra. These fluctuations are typical of supercontinuum generation from PCF modules [38–40]. If left unchecked, the fluctuations from an unstable Stokes supercontinuum can cause detrimental variations in both the observed intensities and peak locations within sequentially obtained CARS spectra, thereby preventing a reliable determination of depolarization ratios. In this work, special care was taken in optimizing

the coupling into the PCF module to ensure that the Stokes spectrum remained as constant and stable as possible in an effort to mitigate any negative impacts caused by unwanted Stokes fluctuations. With optimized coupling, the Stokes supercontinuum remained sufficiently stable on a timescale of an hour or two, to allow a careful measurement of depolarization ratios. In contrast, sub-optimal coupling into the PCF module results in a Stokes supercontinuum that is only stable for a few minutes, and thus is useful only for contrast-based imaging or narrow spectral measurements. As seen in the visualization, the polarization dependence of the emerging spectrum dominates over any Stokes spectral fluctuations. Furthermore, the variation in a given peak's location within each of the 46 benzonitrile CARS spectra is well within the $\sim$30 cm^{-1} spectral resolution of our system and thus negligibly impacts determination of depolarization ratios. Rather than taking an average of the CARS peak locations in each of the 46 benzonitrile spectra, the vibrational frequencies associated with CARS peaks were determined by choosing the frequencies corresponding to maxima in the least-squares fits of the measured total AS intensity as a function of analyzer angle to Eq. (5). Figures 3(a)–(f) present the AS intensity as a function of analyzer angle at five different Raman modes in benzonitrile and at an off-resonance frequency (2450 cm^{-1}). Figures 3(g)–(l) then show the benzonitrile CARS spectra obtained at the indicated analyzer angles in Figs. 3(a)–(f) which roughly correspond to the maximum and minimum fitted AS intensities for the specified vibrational frequency. All fits in Figs. 3(a)–(f) yield R^2 values of 0.95 or better.

Figure 3 and Visualization 1 demonstrate the many polarization dependent features observed in the benzonitrile CARS spectrum using the SFP-CARS method. The different polarizations of the CARS signals observed at 1012 cm^{-1}, 1599 cm^{-1}, and 3059 cm^{-1} is particularly striking, where each of the associated peaks is maximized/minimized at distinctly different analyzer angles. However, the signals appear to be more elliptically polarized than expected. This is evident from the nonzero minimum of AS intensity as a function of analyzer angle at a given vibrational frequency (which is particularly apparent for the 2235 cm^{-1} peak shown in Visualization 1) as well as from the nonzero minima of the fitted AS intensities given by the solid lines in Figs. 3(a)–(f). While on-resonance AS signals are expected to be at least somewhat elliptically polarized due to interference between the non-resonant and resonant responses [36], entirely off-resonance AS signals are expected to be linearly polarized when using linearly polarized pump and Stokes beams. The extinction ratio of the AS signal generated at the off-resonance frequency of 2450 cm^{-1} was measured (by the analyzer) to be approximately 4:1 (see Fig. 3(f)). This is noticeably poorer than the measured extinction ratios of the pump ($ER_\mathrm{p} \approx 23$:1) and Stokes ($ER_\mathrm{s} \approx 52$:1) beams under the microscope without a sample. From this, it seems evident that the microscope and collection optics, as well as possibly the benzonitrile sample itself, contribute to the distortion in the polarizations of the generated signals on route to the detector. This is further supported by the fact that we measure the extinction ratios of the pump and Stokes beams to be $ER_\mathrm{p} \approx 27$:1 and $ER_\mathrm{s} \approx 1000$:1 at the entrance to the microscope and $ER_\mathrm{p} \approx 13$:1 and $ER_\mathrm{s} \approx 64$:1 at the location of the analyzer when the pump and Stokes beams are focused into the benzonitrile sample. For the case of signals generated when probing specific Raman resonances, a combination of polarization distortions caused by microscope and collection optics and interference between non-resonant and resonant signals is likely responsible for the observed elliptical polarizations.

A primary motivation for implementing P-CARS is to suppress the NRB. Figure 3(l) shows the CARS spectra of benzonitrile taken at analyzer angles that roughly correspond to minimum (dark purple line) and maximum (light purple line) extinction of the NRB, respectively. We find that suppression of the NRB is most evident near the 1012 cm^{-1} resonance of benzonitrile (see the dark red arrow in Fig. 3(l)). This is not surprising since the difference between the polarization directions of the non-resonant signal and the signal generated from the 1012 cm^{-1} Raman mode is over 60°. This is easily seen by comparing the locations of the maxima of the curves given in
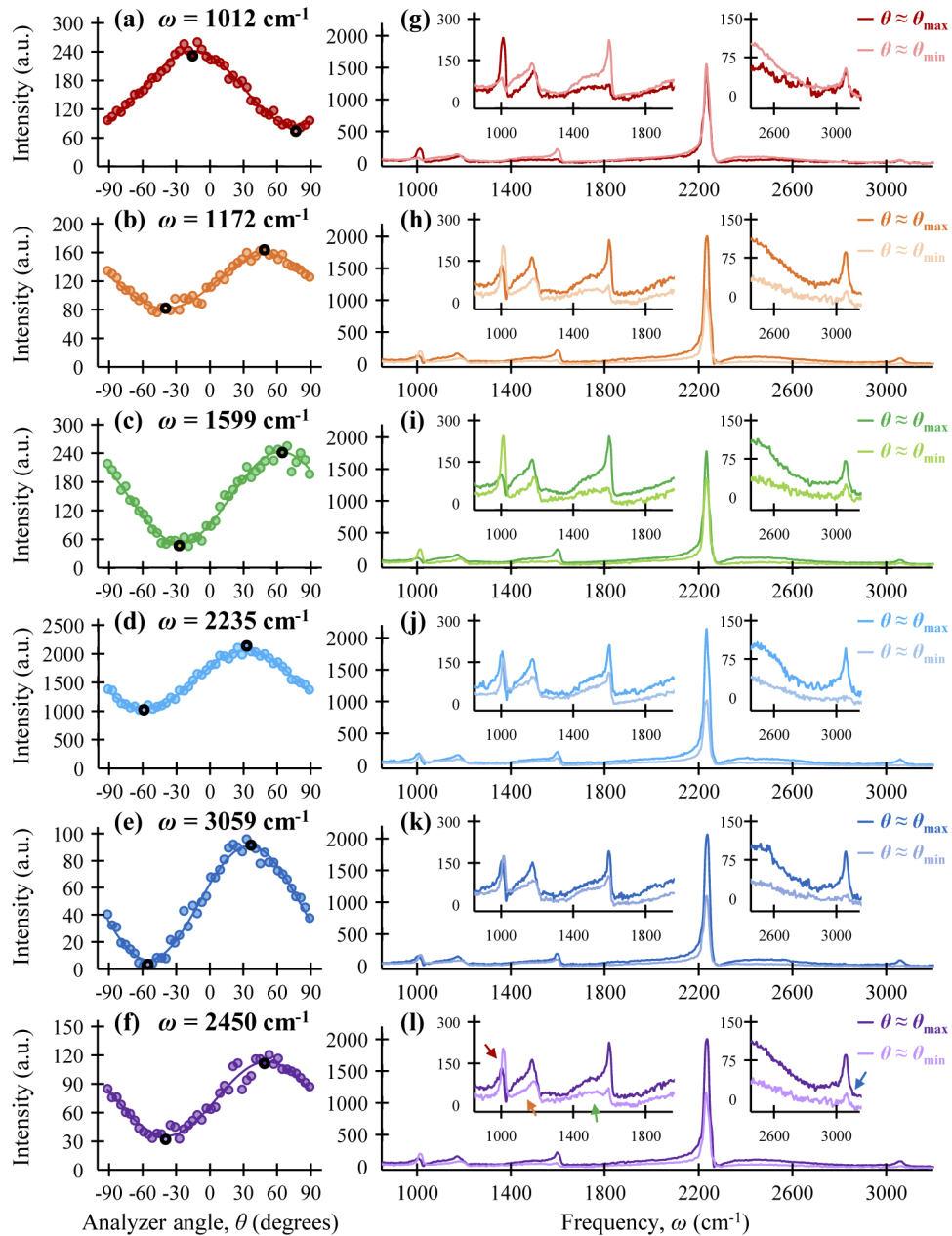
Fig. 3. (a) – (f) Measured total anti-Stokes intensity as a function of analyzer angle, θ, (dots) and corresponding least-squares fits to Eq. (5) (solid lines) when the difference between the pump and Stokes frequencies corresponds to five different resonances in benzonitrile ((a) – (e)) as well as to strong non-resonant AS signal generation at 2450 cm^{-1} (f). Dots with a thick black border signify data taken at analyzer angles of $\theta \approx \theta_{max}$ and $\theta \approx \theta_{min}$ that best match the fitted maximum and minimum signal intensity. (g) – (l) Benzonitrile CARS spectra taken at analyzer angles of $\theta \approx \theta_{max}$ (darker lines) and $\theta \approx \theta_{min}$ (lighter lines) that correspond to the black bordered dots in (a) – (f). The insets in (g) – (l) show magnified portions of the corresponding spectra. The colored arrows in (l) indicate features of interest in the spectrum with the highest NRB suppression, as discussed in the text.

Figs. 3(a) and (f). As such, the non-resonant signal can be suppressed by the analyzer without substantially extinguishing the resonant signal. In the case of the 1012 cm^{-1} resonance, the typical dispersive reshaping of the CARS peak is effectively eliminated by setting the analyzer to suppress the NRB, resulting in a well resolved peak with minimal sacrifice to the overall peak intensity. Generally speaking, however, the NRB suppression across the entire CARS spectrum is unimpressive. Noticeable non-resonant signal is still detected in many portions of the CARS spectrum when the analyzer is rotated for maximum NRB suppression. This is particularly evident near the 1172 cm^{-1} and 1599 cm^{-1} CARS peaks (indicated by the orange and green arrows in Fig. 3(l)). This sub-optimal NRB suppression is likely due to polarization distortion of the non-resonant signal on route to the analyzer. The usefulness of P-CARS for suppressing the NRB is further hindered by the fact that resonant signals polarized in directions close to that of the NRB are also substantially suppressed. This is most clearly observed for the 1599 cm^{-1} and 3059 cm^{-1} resonances (the peaks near the green and blue arrows in Fig. 3(l)) whose corresponding signals appear to be polarized at angles within roughly 16° of that of the NRB. Since this limitation would remain even with much better polarization purity, we conclude that using the analyzer placed after the sample to suppress the NRB is generally only useful when studying Raman modes that generate resonant signals polarized at angles far from the polarization of the NRB. As such, suppression of the NRB in this way using the SFP-CARS system appears to be best suited for on-resonance imaging of specific Raman modes as opposed to obtaining background-free CARS spectra. Even under these circumstances, additional steps should be taken to minimize any altering of signal polarizations caused by optics in the setup before the signals reach the analyzer. Such steps include using lower NA microscope objectives, improving the linear polarizations of the pump and Stokes beams at the sample, and re-designing the system to allow placement of the analyzer immediately after the sample slide.

In principle, the difference between the pump and Stokes polarizations is controlled and set to a known value, but in practice it can also be determined using the dependence of non-resonant AS signal strength on analyzer angle (as shown in Fig. 3(f)). This is done by determining the polarization direction of the non-resonant signal, α, and then substituting this value as well as $\rho_{NR} = 1/3$ into Eq. (1) to determine ϕ. For example, in the present work, the polarization direction of the non-resonant signal is determined to be $\alpha \approx 51°$, as obtained from the maximum of the fit in Fig. 3(f). Substituting this value and $\rho_{NR} = 1/3$ into Eq. (1) yields $\phi \approx 74.9°$ for the difference between the pump and Stokes polarizations at the sample. This matches the value of $\phi \approx 75°$ that was experimentally measured at the location of the analyzer. Evidently, despite polarization distortions caused by optics in the setup, the dependence of non-resonant signal intensity on analyzer angle can still be used to reliably determine the difference between the pump and Stokes polarizations. This is particularly useful if one is unable to experimentally measure the difference between the pump and Stokes polarizations near the location of the sample. Additionally, since ϕ and ρ_{NR} do not depend on the Raman mode being probed, it is clear from Eq. (1) that the polarization direction of the non-resonant signal, α, is expected to be the same across all vibrational frequencies. Our results are consistent with this expectation. For instance, the determined value of α remains within approximately 3° of 51° at off-resonance frequencies from 1750 cm^{-1} to 2150 cm^{-1} and 2400 cm^{-1} to 2800 cm^{-1} where there is sufficient non-resonant signal generation far from any resonances to allow a reliable determination of α. Using Eq. (1) and the measured value of $\phi \approx 75°$, the depolarization ratio of the non-resonant signal generated at frequencies within this range is determined to be within the range $0.30 \lesssim \rho_{NR} \lesssim 0.37$. This is in very good agreement with the theoretically expected value of $\rho_{NR} = 1/3$. Furthermore, this suggests that, while polarization distortions result in CARS signals that are more elliptically polarized than desired for a full suppression of the NRB, the primary polarization directions are sufficiently maintained to allow reliable measurements of Raman depolarization ratios.

Our SFP-CARS system is able to determine Raman depolarization ratios of several resonances of benzonitrile. Table 1 gives the experimentally observed location of each resonance in the CARS spectra of benzonitrile, the polarization angle of each resonant signal, β, extracted from the corresponding fits to Eq. (5), and the associated experimentally determined Raman depolarization ratio, obtained by substituting the corresponding value of β and the measured value of $\phi \approx 75°$ into Eq. (2). Table 1 also gives literature values for the Raman mode locations, and corresponding depolarization ratios, of the Raman resonances in benzonitrile [41]. These literature values are in excellent agreement with the values obtained using a Raman spectroscopy system that we adapted to enable the acquisition of polarized Raman spectra and determine Raman depolarization ratios. Generally speaking, the SFP-CARS system is able to determine the Raman depolarization ratios of various resonances in benzonitrile with a high degree of accuracy. For the 1599 cm^{-1}, 2235 cm^{-1}, and 3059 cm^{-1} Raman modes, the depolarization ratios are determined to be 0.53, 0.17, and 0.19, respectively, which are all within 0.05 of the literature values given in Table 1. This represents excellent agreement given the typical spread and uncertainty in reported Raman depolarization ratios [42]. However, the SFP-CARS-measured values for the depolarization ratios of the 1012 cm^{-1} and 1172 cm^{-1} resonances in benzonitrile are in poorer agreement with those obtained from [41] and warrant further discussion.

Table 1. Vibrational frequencies, values of β, and corresponding depolarization ratios of various Raman resonances in benzonitrile

SFP-CARS values[a]			Literature values[b]	
ω_R (cm^{-1})	β (degrees)	ρ_R	ω_R (cm^{-1})	ρ_R
1012	-15	-0.07	1004	0.04
			1165	0.60
1172	51	0.33	1180	0.10
			1195	0.15
1599	63	0.53	1600	0.52
2235	32	0.17	2226	0.20
3059	35	0.19	3075	0.15

[a]The polarization angle, β, of each resonant signal was experimentally determined by fitting the corresponding signal intensity as a function of analyzer angle to Eq. (5). This value of β and the measured value of $\phi \approx 75°$ were then substituted into Eq. (2) to determine the corresponding Raman depolarization ratio, ρ_R.
[b]The literature Raman frequencies and corresponding depolarization ratios were obtained from the polarized Raman spectra of benzonitrile given in *The Sadtler Standard Raman Spectra, Volume 4* [41]. (The Raman depolarization ratios were obtained from the polarized Raman spectra in the usual way by dividing the perpendicular polarized intensities of the Raman resonances by their corresponding parallel polarized intensities. See [43] for further details.)

In the case of the CARS peak at 1172 cm^{-1}, it is important to note that the Raman spectrum of benzonitrile has three Raman resonances (at 1165 cm^{-1}, 1180 cm^{-1}, and 1195 cm^{-1} [41]) that are all within a 30 cm^{-1} wide window in the region where this single CARS peak is observed. Since the spectral resolution of the SFP-CARS system is approximately 30 cm^{-1}, the setup is unable to resolve these three resonances into separate CARS peaks and thus a single broad peak is observed. Using the dependence of AS intensity on analyzer angle (given in Fig. 3(b)) to determine a Raman depolarization ratio associated with this peak gives a value of approximately 0.33. This is noticeably different from the literature depolarization ratios of the 1165 cm^{-1}, 1180 cm^{-1}, and 1195 cm^{-1} Raman resonances (which are 0.60, 0.10, and 0.15 respectively as given in Table 1). The (unweighted) average of the triplet of depolarization ratios is 0.28 which is in good agreement with our finding of 0.33. As such, the experimentally determined depolarization ratio associated with the 1172 cm^{-1} CARS peak likely originates from a complicated weighted averaging of the depolarization ratios of the three resonances that appear as a single broad CARS peak due to limitations in the spectral resolution of the SFP-CARS setup. Furthermore, it is

likely largely coincidence that the experimentally obtained value of approximately 1/3 is in line with the depolarization ratio of the NRB. Nevertheless and unsurprisingly, we find that the SFP-CARS setup cannot reliably determine the depolarization ratios of resonances that are not clearly resolved as separate CARS peaks. However, it is worth mentioning that without a Raman spectrum of benzonitrile to use for comparison there is no obvious way of knowing that there are three Raman modes in benzonitrile where only a single CARS peak is observed. Therefore, one could erroneously conclude from the observed data that benzonitrile has a Raman resonance at 1172 cm^{-1} with a depolarization ratio that is indistinguishable from that of the NRB.

With regards to the CARS peak at 1012 cm^{-1}, the corresponding Raman depolarization ratio is experimentally determined to be approximately -0.07 which is notably different from the literature depolarization ratio of 0.04. Additionally, a value of -0.07 is outside of the physically allowable range of $0 \leq \rho_R \leq 0.75$ [43]. As it happens, the CARS signals generated at 1012 cm^{-1} originate from the interaction of the pump with a particularly unstable spectral region of the Stokes supercontinuum. Notably, the central frequency of this peak shifts slightly (by as much as 15 cm^{-1}) in each of the 46 spectra, likely as a consequence of these Stokes fluctuations. Further analysis in which the peak location of this resonance is fixed at 1012 cm^{-1} yields a similar value of -0.05 for the depolarization ratio. Thus, it is unlikely that such frequency shifts are the reason that we obtain an unphysical (negative) depolarization ratio for this peak. Instead, we believe that the discrepancy is primarily due to an increased influence of interference between the non-resonant and resonant signals. This interference causes a slight shift in the polarization direction of the total AS signal compared to that of the resonant signal resulting in a depolarization ratio determined using the approximation given by Eq. (5) in combination with Eq. (2) that differs from the true value. The increased impact of interference is likely due to a combination of the non-resonant signal strength being closer to that of the resonant signal and the non-resonant and resonant signals having a phase difference, δ, that enhances the influence of the interference term in the expression for the total AS intensity as a function of analyzer angle given by Eq. (3). Nevertheless, one can still reasonably and correctly conclude that the 1012 cm^{-1} resonance is a highly symmetric mode since its depolarization ratio is very close to zero [43]. While the value obtained using the SFP-CARS system is ultimately unphysical, experimental imprecisions can lead to slight negative deviations in determined depolarization ratios and discrepancies greater than that observed for the 1012 cm^{-1} resonance are not uncommon between depolarization ratios reported in the literature [42].

A final consideration in the SFP-CARS system is that of residual pump and Stokes signal leakage reaching the detector. In Fig. 4 and Visualization 2, we show the benzonitrile CARS spectrum taken at various analyzer angles without subtraction of residual pump and Stokes "leakage". The strength and polarization dependence of this unwanted background signal is highlighted particularly well by Visualization 2. By examining the pump and Stokes leakage separately, we find that the pump leakage when the analyzer is set to allow maximum pump transmission is roughly ten times greater than the Stokes leakage when the analyzer is set to allow maximum Stokes transmission. Therefore, the total leakage signal is dominated by pump leakage and thus appears to be polarized in roughly the same direction as the pump. Since the pump leakage is still significant despite the many filters placed after the analyzer in the setup (see Fig. 2), we conclude that the pump leakage likely originates from the tail of the pump spectrum at wavelengths just below the cutoff of the 785 nm short-pass filter. In any case, the adaptation of the setup to allow polarization sensitive detection evidently results in weaker detected non-resonant and resonant AS signals, with intensities that are comparable to or exceeded by the intensities of the pump and Stokes leakage signals reaching the detector. For comparison, the maximum pump leakage intensity is roughly 75% of the maximum peak height of the 2235 cm^{-1} peak shown in Fig. 3(j) while the maximum Stokes leakage intensity is roughly 70% of the maximum peak height of the 1012 cm^{-1} peak shown in Fig. 3(g). These residual

pump and Stokes signals are a substantial hindrance to contrast-based imaging capabilities of the SFP-CARS setup because of the need to subtract the unwanted pump and Stokes leakage from each pixel. Otherwise, non-resonant, or potentially even resonant, AS signals may be drowned out by the undesirable pump and Stokes signals reaching the detector. Furthermore, it is critical that these residual signals are accounted for to obtain accurate polarization sensitive information, including Raman depolarization ratios. In all, we conclude that while the unwanted leakage hinders contrast in imaging, it does not inhibit spectral processing, peak identification, and extraction of depolarization ratios as long as it is properly considered.
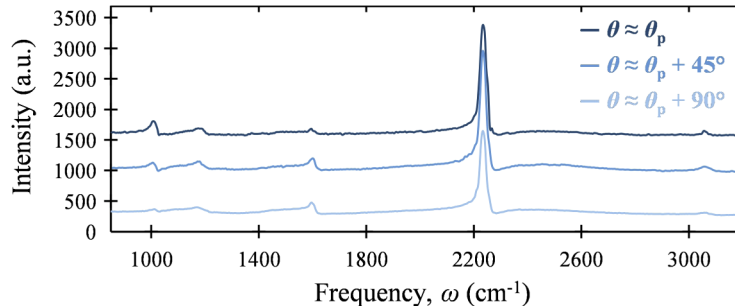

Fig. 4. Benzonitrile CARS spectra taken at the indicated analyzer angles, θ, without subtracting the residual pump and Stokes intensities reaching the detector. The spectra have not been shifted vertically. Thus, the baseline leakage is approximately 5 times as large when the analyzer transmission angle is aligned to the pump polarization ($\theta = \theta_p$) than when they are orthogonal ($\theta = \theta_p + 90°$).

5. Conclusion

We have described and assessed the capabilities of a novel spectral-focusing-based polarization-resolved CARS (SFP-CARS) microscopy system, developed by making simple modifications to an existing SF-CARS setup. While the detected AS signals are more elliptically polarized than expected, likely due to polarization distortions caused by microscope and collection optics in the setup, we find that the system is able to reliably determine the depolarization ratios of various Raman modes in benzonitrile. We demonstrated that by fitting the signal intensity as a function of analyzer angle, the depolarization ratios of the 1599 cm^{-1}, 2235 cm^{-1}, and 3059 cm^{-1} Raman modes can be determined to within 0.05 of the corresponding literature values. In the case of the 1012 cm^{-1} resonance in benzonitrile, the obtained value of -0.07 is similar to the literature value of 0.04, but is ultimately unphysical. This discrepancy is likely due to an increased influence of interference between the non-resonant and resonant AS signals on the polarization direction of the total AS signal. Nevertheless, we present a simple and accurate means of determining depolarization ratios for strong Raman resonances. For weak Raman resonances, the SFP-CARS setup should still be able to accurately determine the associated depolarization ratios, but this would require the use of additional techniques, such as phase retrieval algorithms, to separate the non-resonant and resonant signal intensities.

Traditionally, P-CARS methods have been motivated as a means of eliminating the effects of the NRB. We find that despite considerable efforts to reduce elliptical polarization components and incident beam leakage, noticeable non-resonant signal is still detected in many regions of the CARS spectrum when the analyzer is perpendicular to the polarization of the non-resonant signal. This is likely due to polarization distortions of the non-resonant signals caused by optics in the setup. Furthermore, we find that the resonant signals originating from the 1599 cm^{-1} and 3059 cm^{-1} resonances in benzonitrile are also substantially suppressed when the analyzer is set

to extinguish the NRB because these resonant signals are polarized in directions similar to that of the NRB. While NRB suppression is effective for the 1012 cm^{-1} resonance in benzonitrile, we find that the drawbacks of implementing polarization control and detection outweigh any benefits in terms of NRB suppression. We conclude that suppressing the NRB using the SFP-CARS system is best suited for imaging specific Raman modes that generate resonant signals polarized in directions far from that of the NRB instead of for obtaining background-free CARS spectra.

In all, we find that the SFP-CARS setup described in this work is a useful and promising tool for studying polarization dependent features in the CARS spectra of various samples. We have demonstrated that by making relatively simple and low-cost modifications a conventional SF-CARS setup can be adapted to extract valuable polarization sensitive information from samples and determine Raman depolarization ratios. Ultimately, imaging variations in depolarization ratios could add important information regarding the local microstructure and organization of biomaterials and tissues. We have presented an approach that can enable such microscopy in timescales far shorter than are available with polarization-resolved spontaneous Raman systems.

Disclosures

The authors declare no conflicts of interest.

References

1. C. L. Evans and X. S. Xie, "Coherent anti-Stokes Raman scattering microscopy: chemical imaging for biology and medicine," Annu. Rev. Anal. Chem. **1**(1), 883–909 (2008).
2. A. Volkmer, "Vibrational imaging and microspectroscopies based on coherent anti-Stokes Raman scattering microscopy," J. Phys. D: Appl. Phys. **38**(5), R59–R81 (2005).
3. M. Müller and A. Zumbusch, "Coherent anti-Stokes Raman scattering microscopy," ChemPhysChem **8**, 2156–2170 (2007).
4. J.-X. Cheng and X. S. Xie, "Coherent anti-Stokes Raman scattering microscopy: instrumentation, theory, and applications," J. Phys. Chem. B **108**(3), 827–840 (2004).
5. T. Hellerer, A. M. K. Enejder, and A. Zumbusch, "Spectral focusing: high spectral resolution spectroscopy with broad-bandwidth laser pulses," Appl. Phys. Lett. **85**(1), 25–27 (2004).
6. J. G. Porquez, R. A. Cole, J. T. Tabarangao, and A. D. Slepkov, "Spectrally-broad coherent anti-Stokes Raman scattering hyper-microscopy utilizing a Stokes supercontinuum pumped at 800 nm," Biomed. Opt. Express **7**(10), 4335–4345 (2016).
7. H. Tu, Y. Liu, D. Turchinovich, M. Marjanovic, J. K. Lyngsø, J. Lægsgaard, E. J. Chaney, Y. Zhao, S. You, W. L. Wilson, B. Xu, M. Dantus, and S. A. Boppart, "Stain-free histopathology by programmable supercontinuum pulses," Nat. Photonics **10**(8), 534–540 (2016).
8. A. D. Slepkov, A. Ridsdale, H.-N. Wan, M.-H. Wang, A. F. Pegoraro, D. J. Moffatt, J. P. Pezacki, F.-J. Kao, and A. Stolow, "Forward-collected simultaneous fluorescence lifetime imaging and coherent anti-Stokes Raman scattering microscopy," J. Biomed. Opt. **16**(2), 021103 (2011).
9. K. P. Herdzik, K. N. Bourdakos, P. B. Johnson, A. P. Lister, A. P. Pitera, C. Guo, P. Horak, D. J. Richardson, J. H. V. Price, and S. Mahajan, "Multimodal spectral focusing CARS and SFG microscopy with a tailored coherent continuum from a microstructured fiber," Appl. Phys. B **126**(5), 84 (2020).

10. R. A. Cole and A. D. Slepkov, "Interplay of pulse bandwidth and spectral resolution in spectral-focusing CARS microscopy," J. Opt. Soc. Am. B **35**(4), 842–850 (2018).

11. W. Langbein, I. Rocha-Mendoza, and P. Borri, "Coherent anti-Stokes Raman micro-spectroscopy using spectral focusing: theory and experiment," J. Raman Spectrosc. **40**, 800–808 (2009).

12. J. G. Porquez and A. D. Slepkov, "Application of spectral-focusing-CARS microscopy to pharmaceutical sample analysis," AIP Adv. **8**(9), 095213 (2018).

13. B.-C. Chen, J. Sung, X. Wu, and S.-H. Lim, "Chemical imaging and microspectroscopy with spectral focusing coherent anti-Stokes Raman scattering," J. Biomed. Opt. **16**(2), 021112 (2011).

14. A. F. Pegoraro, A. D. Slepkov, A. Ridsdale, D. J. Moffatt, and A. Stolow, "Hyperspectral multimodal CARS microscopy in the fingerprint region," J. Biophotonics **7**, 49–58 (2014).

15. I. Pope, W. Langbein, P. Watson, and P. Borri, "Simultaneous hyperspectral differential-CARS, TPF and SHG microscopy with a single 5 fs Ti:Sa laser," Opt. Express **21**(6), 7096–7106 (2013).

16. J.-X. Cheng, A. Volkmer, and X. S. Xie, "Theoretical and experimental characterization of coherent anti-Stokes Raman scattering microscopy," J. Opt. Soc. Am. B **19**(6), 1363–1375 (2002).

17. A. Zeytunyan, K. T. Crampton, R. Zadoyan, and V. A. Apkarian, "Supercontinuum-based three-color three-pulse time-resolved coherent anti-Stokes Raman scattering," Opt. Express **23**(18), 24019–24028 (2015).

18. P. K. Upputuri, L. Gong, and H. Wang, "Chirped time-resolved CARS microscopy with square-pulse excitation," Opt. Express **22**(8), 9611–9626 (2014).

19. Y. J. Lee, S. H. Parekh, Y. H. Kim, and M. T. Cicerone, "Optimized continuum from a photonic crystal fiber for broadband time-resolved coherent anti-Stokes Raman scattering," Opt. Express **18**(5), 4371–4379 (2010).

20. Y. Liu, Y. J. Lee, and M. T. Cicerone, "Broadband CARS spectral phase retrieval using a time-domain Kramers–Kronig transform," Opt. Lett. **34**(9), 1363–1365 (2009).

21. B.-R. Lee, K.-I. Joo, E. S. Choi, J. Jahng, H. Kim, and E. Kim, "Evans blue dye-enhanced imaging of the brain microvessels using spectral focusing coherent anti-Stokes Raman scattering microscopy," PLoS One **12**(10), e0185519 (2017).

22. C. H. Camp Jr., Y. J. Lee, and M. T. Cicerone, "Quantitative, comparable coherent anti-Stokes Raman scattering (CARS) spectroscopy: correcting errors in phase retrieval," J. Raman Spectrosc. **47**, 408–415 (2016).

23. J.-L. Oudar, R. W. Smith, and Y. R. Shen, "Polarization-sensitive coherent anti-Stokes Raman spectroscopy," Appl. Phys. Lett. **34**(11), 758–760 (1979).

24. J.-X. Cheng, L. D. Book, and X. S. Xie, "Polarization coherent anti-Stokes Raman scattering microscopy," Opt. Lett. **26**(17), 1341–1343 (2001).

25. M. Hofer, N. K. Balla, and S. Brasselet, "High-speed polarization-resolved coherent Raman scattering imaging," Optica **4**(7), 795–801 (2017).

26. P. Gasecka, A. Jaouen, F.-Z. Bioud, H. B. de Aguiar, J. Duboisset, P. Ferrand, H. Rigneault, N. K. Balla, F. Debarbieux, and S. Brasselet, "Lipid Order Degradation in Autoimmune Demyelination Probed by Polarized Coherent Raman Microscopy," Biophys. J. **113**(7), 1520–1530 (2017).

27. F. Munhoz, S. Brustlein, D. Gachet, F. Billard, S. Brasselet, and H. Rigneault, "Raman depolarization ratio of liquids probed by linear polarization coherent anti-Stokes Raman spectroscopy," J. Raman Spectrosc. **40**(7), 775–780 (2009).

28. T. Würthwein, M. Brinkmann, T. Hellwig, and C. Fallnich, "Rapid spectro-polarimetry to probe molecular symmetry in multiplex coherent anti-Stokes Raman scattering," J. Chem. Phys. **147**(19), 194201 (2017).

29. A. F. Pegoraro, A. Ridsdale, D. J. Moffatt, Y. Jia, J. P. Pezacki, and A. Stolow, "Optimally chirped multimodal CARS microscopy based on a single Ti:sapphire oscillator," Opt. Express **17**(4), 2984–2996 (2009).

30. J.-X. Cheng, A. Volkmer, L. D. Book, and X. S. Xie, "Multiplex coherent anti-Stokes Raman scattering microspectroscopy and study of lipid vesicles," J. Phys. Chem. B **106**(34), 8493–8498 (2002).

31. C. H. Camp Jr., Y. J. Lee, J. M. Heddleston, C. M. Hartshorn, A. R. H. Walker, J. N. Rich, J. D. Lathia, and M. T. Cicerone, "High-speed coherent Raman fingerprint imaging of biological tissues," Nat. Photonics **8**(8), 627–634 (2014).

32. R. W. Boyd, *Nonlinear Optics*, 3rd ed. (Academic Press, 2008).

33. W. M. Tolles, J. W. Nibler, J. R. McDonald, and A. B. Harvey, "A Review of the Theory and Application of Coherent Anti-Stokes Raman Spectroscopy (CARS)," Appl. Spectrosc. **31**(4), 253–271 (1977).

34. S. Brasselet, "Polarization-resolved nonlinear microscopy: application to structural molecular and biological imaging," Adv. Opt. Photonics **3**(3), 205–271 (2011).

35. J. P. R. Day, K. F. Domke, G. Rago, H. Kano, H. Hamaguchi, E. M. Vartiainen, and M. Bonn, "Quantitative coherent anti-Stokes Raman scattering (CARS) microscopy," J. Phys. Chem. B **115**(24), 7713–7725 (2011).

36. S. A. Akhmanov, A. F. Bunkin, S. G. Ivanov, and N. I. Koroteev, "Polarization active Raman spectroscopy and coherent Raman ellipsometry," Sov. J. Exp. Theor. Phys. **47**, 667–678 (1978).

37. The value of 0.1 is determined by comparing the value of ρ_R obtained using the angle corresponding to the maximum of Eq. (3) as the value of β in Eq. (2) with the true value of ρ_R obtained using the correct value of β in Eq. (2) for a variety of allowed β values with $|\chi^{(3)R}| = 10|\chi^{(3)NR}|$ (such that $I^R_{AS_0} = 100 I^{NR}_{AS_0}$), $\alpha = 45°$, $\phi = 71.6°$, and maximum constructive ($\delta = 0$) or destructive ($\delta = \pi$) interference between the non-resonant and resonant AS signals.

38. J. G. Porquez, R. A. Cole, and A. D. Slepkov, "Comparison of two photonic crystal fibers for supercontinuum-Stokes spectral-focusing-CARS hyperspectroscopy," OSA Continuum **1**(4), 1385–1399 (2018).

39. M. Naji, S. Murugkar, and H. Anis, "Determining optimum operating conditions of the polarization-maintaining fiber with two far-lying zero dispersion wavelengths for CARS microscopy," Opt. Express **22**(9), 10800–10814 (2014).

40. S. Gagliardi, M. Marrocco, F. Rondino, D. Palumbo, C. Merla, and M. Falconieri, "Studies of supercontinuum generation in a photonic crystal fiber for use as Stokes beam in a single-laser femtosecond micro-CARS setup," J. Raman Spectrosc. **Early Access**, 1–8 (2020).

41. . *Standard Raman Spectra, Volume 4* (Sadtler Research Laboratories, 1974).

42. J. Kiefer, "Simultaneous Acquisition of the Polarized and Depolarized Raman Signal with a Single Detector," Anal. Chem. **89**(11), 5725–5728 (2017).

43. D. P. Strommen, "Specific values of the depolarization ratio in Raman spectroscopy: Their origins and significance," J. Chem. Educ. **69**(10), 803–807 (1992).